

Fabrication-induced even-odd discrepancy of magnetotransport in few-layer MnBi₂Te₄

Yaoxin Li^{1,*}, Yongchao Wang^{1,*}, Zichen Lian^{1,*}, Hao Li^{2,3}, Zhiting Gao⁴, Liangcai Xu¹,
Huan Wang^{5,6}, Rui'e Lu⁷, Longfei Li⁸, Yang Feng⁶, Jinjiang Zhu⁹, Liangyang Liu¹,
Yongqian Wang^{5,6}, Bohan Fu^{5,6}, Shuai Yang^{5,6}, Luyi Yang^{1,10}, Yihua Wang^{9,11}, Tianlong
Xia^{5,6}, Chang Liu¹², Shuang Jia^{8,13,14}, Yang Wu¹⁵, Jinsong Zhang^{1,10,16}, Yayu Wang^{1,10,16},
Chang Liu^{5,6†}

¹*State Key Laboratory of Low Dimensional Quantum Physics, Department of Physics,
Tsinghua University, Beijing 100084, China*

²*School of Materials Science and Engineering, Tsinghua University, Beijing 100084, China*

³*Tsinghua-Foxconn Nanotechnology Research Center, Department of Physics, Tsinghua
University, Beijing 100084, China*

⁴*Beijing Academy of Quantum Information Sciences, Beijing 100193, China*

⁵*Beijing Key Laboratory of Opto-electronic Functional Materials & Micro-Nano Devices,
Department of Physics, Renmin University of China, 100872 Beijing, China*

⁶*Key Laboratory of Quantum State Construction and Manipulation (Ministry of Education),
Renmin University of China, Beijing 100872, China*

⁷*School of Mechanical and Electric Engineering, Guangzhou University, Guangzhou
510006, China*

⁸*International Center for Quantum Materials, School of Physics, Peking University, Beijing
100871, China*

⁹*State Key Laboratory of Surface Physics and Department of Physics, Fudan University,
Shanghai 200433, China*

¹⁰*Frontier Science Center for Quantum Information, Beijing 100084, China*

¹¹*Shanghai Research Center for Quantum Sciences, Shanghai 201315, China.*

¹²*Shenzhen Institute for Quantum Science and Engineering and Department of Physics,
Southern University of Science and Technology, Shenzhen 518055, China*

¹³*Interdisciplinary Institute of Light-Element Quantum Materials and Research Center
for Light-Element Advanced Materials, Peking University, Beijing 100871, China*

¹⁴*CAS Center for Excellence in Topological Quantum Computation, University of
Chinese Academy of Sciences, Beijing 100190, China*

¹⁵*College of Math and Physics, Beijing University of Chemical Technology, Beijing
100029, China*

¹⁶*Hefei National Laboratory, Hefei 230088, China*

* These authors contributed equally to this work.

† Emails: liuchang_phy@ruc.edu.cn

The van der Waals antiferromagnetic topological insulator MnBi_2Te_4 represents a promising platform for exploring the layer-dependent magnetism and topological states of matter. Recently observed discrepancies between magnetic and transport properties have aroused controversies concerning the topological nature of MnBi_2Te_4 in the ground state. In this article, we demonstrate that fabrication can induce mismatched even-odd layer dependent magnetotransport in few-layer MnBi_2Te_4 . We perform a comprehensive study of the magnetotransport properties in 6- and 7-septuple-layer MnBi_2Te_4 , and reveal that both even- and odd-number-layer device can show zero Hall plateau phenomena in zero magnetic field. Importantly, a statistical survey of the optical contrast in more than 200 MnBi_2Te_4 flakes reveals that the zero Hall plateau in odd-number-layer devices arises from the reduction of the effective thickness during the fabrication, a factor that was rarely noticed in previous studies of 2D materials. Our finding not only provides an explanation to the controversies regarding the discrepancy of the even-odd layer dependent magnetotransport in MnBi_2Te_4 , but also highlights the critical issues concerning the fabrication and characterization of 2D material devices.

Introduction

The antiferromagnetic (AFM) topological insulator (TI) MnBi_2Te_4 provides promising opportunities for exploring various quantized topological phenomena¹⁻⁶. As a layered *A*-type antiferromagnet, MnBi_2Te_4 bulk crystal is composed of septuple layers (SLs) stacked along the *c*-axis with intralayer ferromagnetic (FM) order and interlayer AFM order (Fig. 1a). The interplay between magnetic order and band topology gives rise to gapped surface states that exhibit half-quantized surface Hall conductivity $\sigma_{xy} = 0.5 e^2/h$, where h represents the Plank constant and e denotes the elementary charge^{7,8}. Therefore, depending on the magnetizations of the top and bottom surfaces, few-layer MnBi_2Te_4 with different SL-number-parity exhibits distinct topological quantum states⁹. In odd-number-SL MnBi_2Te_4 , the parallel magnetization on the two surfaces gives rise to the quantum anomalous Hall (QAH) effect^{3,10} characterized by quantized Hall resistivity (ρ_{yx}) and vanished longitudinal resistivity (ρ_{xx}) at zero magnetic field (H). In contrast, even-number-SL MnBi_2Te_4 displays a robust zero Hall plateau $\rho_{yx} = 0$

and large ρ_{xx} in a wide range of both $\mu_0 H$ and gate voltage (V_g), as the counter-propagating Hall currents in the two surfaces cancel out¹¹⁻¹³. Because the zero Hall plateau with Chern number $C = 0$ is closely related to the topological magnetoelectric effect that stems from the axion electrodynamics¹⁴⁻¹⁶, magnetic TI with antiparallel magnetizations of two surfaces is widely believed as an ideal system for realizing the axion insulator state^{5,17-19}. Recently, using a circularly polarized light, the axion electrodynamics has been detected in a 6-SL MnBi_2Te_4 in the zero Hall plateau regime²⁰.

Despite the experimental demonstration of the QAH effect and the axion insulator state, the fabrication of high-quality MnBi_2Te_4 devices with expected quantized properties remains a key challenge. In previous experiments, most odd-number-SL MnBi_2Te_4 exhibited a small AH effect that is far from quantization^{3,21,22}, while even-number-SL devices usually exhibited linear normal Hall effect with negative slope in the AFM regime^{4,23}. More puzzlingly, recent magnetic and transport measurements²⁴⁻²⁷ found that the AH effect disappeared in some odd-number-SL MnBi_2Te_4 with uncompensated AFM order, whereas a pronounced AH hysteresis occurred in some even-number-SL devices with fully compensated AFM order. Interestingly, the chirality of the AH hysteresis is opposite to the expected clockwise chirality for Mn-based TIs²⁸⁻³⁰. These counter-intuitive results have aroused widespread controversies regarding the topological nature of MnBi_2Te_4 in the AFM state, significantly impeding the explorations of other exotic topological quantum phenomena in topological antiferromagnets^{14-16,31}. Several distinct scenarios have been proposed to account for these anomalies, such as the competition between intrinsic and extrinsic mechanisms of AH effect³², the magnetoelectric effect from the orbital magnetization³³, and the layer-dependent hidden Berry curvature³⁴. However, all the ideas assume MnBi_2Te_4 crystals with perfect sample qualities and electronic structure. As has been demonstrated by experiments³⁵⁻³⁷, even starting with the most optimized crystal, the electronic structure of a fabricated device may change dramatically, which is a critical issue in Bi_2Te_3 family TI materials. Theoretical calculations also suggested that the surface defects can result in redistribution of the surface charge from the first layer toward the second layer³⁸, which will modify the magnetotransport performance of few-layer MnBi_2Te_4 . Consequently, a promising yet unexplored research direction is to elucidate whether the fabrication process

can lead to distinct transport behaviors in MnBi_2Te_4 , which may offer a novel perspective for resolving the discrepancies in previous experiments.

In this work, we report systematic magnetotransport studies and the evolution of optical contrast (O_c) on 223 MnBi_2Te_4 devices with varied thickness. All the seven transport devices (from 5 SL to 8 SL) manifest quantized $\rho_{yx} \sim h/e^2$ in the field-polarized Chern insulator state, suggesting the high quality of our MnBi_2Te_4 devices. We demonstrate that fabrication process can result in mismatched even-odd layer dependent magnetotransport in few-layer MnBi_2Te_4 . A comprehensive study of the magnetotransport behaviors in a 6- and 7-SL device shows that both even- and odd-number-SL MnBi_2Te_4 can exhibit zero Hall plateau in zero magnetic field. A statistical survey of the O_c in more than 200 MnBi_2Te_4 reveals that the effective thickness for magnetotransport could decrease by 1 SL after undergoing the electron-beam-lithography (EBL) method. Our finding not only provides an explanation to the controversies concerning the even-odd discrepancy of magnetotransport in few-layer MnBi_2Te_4 , but also highlights the critical issues regarding the fabrication and characterization of 2D material devices.

Results

Device Fabrication and Basic Calibration of Transport Properties

MnBi_2Te_4 few-layer flakes were prepared via mechanical exfoliation on 285 nm SiO_2/Si substrates (see methods section). We then determined the thickness of the flakes using optical methods (Fig. 1b), atomic force microscopy (Fig. 1c) and scanning superconducting quantum interference device (SQUID) (see supplementary section A). The calibration of thickness was also examined by additional layer-dependent measurements on flakes exfoliated from crystal #1, including nonlocal transport, scanning microwave impedance microscopy (sMIM), ultra-fast pump-probe reflectivity, and Raman spectroscopy^{13,39-41}. By conducting O_c measurement immediately after exfoliation in a glovebox, one can quickly determine the thickness without exposing the sample to the atmosphere. Figure 1d summarizes the one-to-one correspondence between O_c and thickness (SL number), which are highly consistent with the results measured in different crystals by another group²³. For few-layer MnBi_2Te_4 , a remarkable feature is that O_c changes its sign from negative to positive when the thickness increases from 6 SL to 7 SL,

as guided by the dashed line. After the identification of thickness, the flakes were fabricated into field-effect-transistors by standard EBL method and coated with a layer of Polymethyl Methacrylate (PMMA) for protection (see supplementary section A for details). To study the layer-dependent transport properties, we first measured the temperature (T) dependent ρ_{xx} for a 6-SL and 7-SL device (S2 and S6) at $\mu_0H = 0$, with the Fermi levels (E_{FS}) gated to the charge neutrality points (CNPs). Both the two flakes were derived from crystal #1. At the CNP, the transport is mainly conducted by the topological surface states or edge states. Therefore, both devices exhibit overall insulating behavior and display kink feature at their Néel temperatures (T_{NS}). Compared to $T_N \sim 25$ K for MnBi_2Te_4 bulk crystals⁵, the T_{NS} for the few-layer devices are suppressed to 20.6 K and 21.6 K, respectively, possibly due to the enhanced fluctuations at lower dimensions.

Layer-dependent Magnetoelectric Transport Properties for Varied V_g

As a layered AFM TI, the most intriguing feature of MnBi_2Te_4 is the layer-dependent transport properties. We performed systematic μ_0H dependent transport measurements on the two devices at different V_g s (see supplementary section B for transport data at various T s), as presented in Figs. 2a and 2b. With the application of V_g , E_F is continuously tuned from the valence band towards the conduction band, manifested by the slope change of normal Hall effect from positive to negative. For the 6-SL MnBi_2Te_4 , the most remarkable feature lies in the broad zero Hall plateau in the low-field AFM regime when its E_F is tuned within the band gap. In the panels enclosed by thick magenta boundaries, the zero Hall plateau persists in a wide range of V_g from 36 to 49 V. Meanwhile, ρ_{xx} shows insulating behavior and reaches as high as $4 h/e^2$. These behaviors are indicative of the axion insulator state in even-number-SL MnBi_2Te_4 , where the counter-propagating surface Hall currents give rise to a broad zero Hall plateau in ρ_{yx} and a large ρ_{xx} (ref. ^{5,12,13}). An out-of-plane μ_0H drives the system into a Chern insulator at the CNP ($V_g = 42$ V), where ρ_{yx} is quantized in h/e^2 and ρ_{xx} drops to zero for $\mu_0H > 6$ T. These behaviors are consistent with previous reports on the topological phase transition between axion insulator and Chern insulator in a 6-SL device^{5,20}.

Figure 2b shows the μ_0H -dependent ρ_{yx} and ρ_{xx} at various V_g s for the 7-SL device, which

exhibit unexpected zero Hall plateau phenomenon rather than AH hysteresis in the AFM state. At high field, the 7-SL device show transport behaviors very similar to the 6-SL device with quantized ρ_{yx} and vanished ρ_{xx} , as the Chern insulator quantization in the FM state does not depend on thickness. However, in the low-field AFM regime, some unexpected behaviors are observed. As guided by the black dashed lines, throughout the V_g range, ρ_{yx} displays overall linear behaviors and smoothly changes the slope from positive to negative. No discernable hysteresis is observed during the field sweep process. Remarkably, at $V_g = 13$ V, a wide zero Hall plateau appears between $\mu_0 H = \pm 3$ T. Meanwhile, ρ_{xx} reaches the maximum but with a smaller value than that of the 6-SL device. Theoretically, the zero Hall plateau phenomenon is unique to even-number-SL MnBi_2Te_4 with fully compensated AFM order, thus should be absent in odd-number-SL MnBi_2Te_4 . These unexpected results strongly suggest the existence of some unknown mechanism that could modify the magnetotransport of few-layer MnBi_2Te_4 .

In order to realize the QAH and axion insulator state in few-layer MnBi_2Te_4 , E_F must be tuned by V_g to lie in the Dirac point gap opened by FM order. To reveal the nature of the zero Hall phenomena in the two devices, we extract the value of ρ_{xx} and the slope of ρ_{yx} at $\mu_0 H = 0$, and plot them as a function of V_g . As displayed in Fig. 3a, ρ_{xx} of the 6-SL device first goes up to a large value of $4 h/e^2$ for $V_g < 25$ V and remains unchanged in a broad V_g window, and then decreases to a small value for $V_g > 50$ V. Meanwhile, $d\rho_{yx}/dH$ exhibits a clear three-stage transition with varying V_g . In the first stage with $V_g < 30$ V, $d\rho_{yx}/dH$ progressively decreases with increasing V_g , and is attributed to the depletion of hole-type carriers. For V_g from 25 to 30 V, $d\rho_{yx}/dH$ changes sign from positive to negative. As V_g is further increased, a broad zero plateau forms and persists within a V_g window of 13 V. Further application of V_g injects more electron-type carriers and ultimately leads to negative $d\rho_{yx}/dH$. Such behaviors unequivocally suggest that the zero Hall plateau state in the 6-SL MnBi_2Te_4 is a genuine quantized Hall state ($C = 0$) with E_F residing in the band gap, which is consistent with our previous report⁵.

Despite the superficially similar zero Hall plateau during $\mu_0 H$ sweep in the 7-SL device, it manifests different behavior in response to V_g . In contrast to the 6-SL device where $d\rho_{yx}/dH = 0$ exists in a broad V_g window, for the 7-SL device, $d\rho_{yx}/dH = 0$ only appears at a single V_g point corresponding to the sign change of ρ_{yx} slope. Meanwhile, we notice that for the 6-SL

device, there is a broad V_g range where the zero Hall plateau and the Chern insulator coexist. However, for the 7-SL device, the zero Hall plateau only occurs in a V_g smaller than the Chern insulator regime (see supplementary section C for colormaps of ρ_{yx} and ρ_{xx}). For longitudinal transport, the V_g range for large ρ_{xx} in the 7-SL device is also narrower than the 6-SL device. To better visualize the different manifestations of the zero Hall plateaus, we summarize the variations of $d\rho_{yx}/dH$ with V_g and μ_0H for the two devices to two colormaps, as shown in Figs. 3c and 3d. The magenta dashed lines label the regimes for $d\rho_{yx}/dH = 0$. It clearly shows that there is a well-defined zero Hall resistivity plateau regime in the parameter space for the 6-SL device. However, for the 7-SL device, the zero Hall plateau exists in a narrower regime. The quantitative differences of the zero Hall plateaus in the V_g range, as well as that in the T range (see supplementary Fig. S4), indicate different manifestations of the zero Hall plateau associated with the axion insulator state of different energy gaps.

The observation of zero Hall plateau phenomenon in the 7-SL device bears resemblance to a recent observation of the discrepancies between magnetic order and transport properties in few-layer MnBi_2Te_4 , where the absence of AH effect was observed in a 5-SL device with uncompensated AFM order, meanwhile a pronounced AH effect was found in a 6-SL device with fully compensated AFM order^{24,25}. Previous magnetic measurements have demonstrated that the AFM order in MnBi_2Te_4 is highly robust and persist to the top surface^{42,43}. In contrast, the surface electronic band structures have been found to be fragile and sensitive to the type and concentration of defects^{38,44-47}. We notice that most of the magnetization measurements in previous reports^{24,25} were performed on MnBi_2Te_4 with fresh surface, whereas the transport measurements were conducted exclusively in devices after fabrication. It is highly possible that the even-odd discrepancy of magnetotransport in MnBi_2Te_4 arises from the influences of fabrication process. To verify our conjecture, we tracked the O_c values measured before and after fabrication for the two devices, as illustrated in Figs. 3c and 3d. Surprisingly, we find a substantial O_c reduction from +12.5 to -0.2 % for the 7-SL device after fabrication, indicating that the thickness determined by O_c is significantly reduced by 1 SL. In contrast, the O_c value of the 6-SL device is less influenced, only changing slightly from -7.4 to -10.0 %.

Statistical Survey of Optical Properties and its Effects on Charge Transport

In order to figure out the reason for the color change and to exclude any artificial factor that may contribute to our observation, such as the transport electrodes, fabrication conditions, and imaging parameters *etc.*, we conducted thorough control experiments on many few-layer flakes and compared O_c changes under different conditions (see supplementary section D for details). To mitigate the potential interferences from extrinsic effects, such as thermal cycling, environmental doping, and aging effect, O_c was obtained immediately after surface treatment in a glovebox^{36,37,48,49}. Of the many relevant factors, we notice that the contact with PMMA plays the most crucial role on the reduction of O_c , a factor that was rarely noticed in previous studies of 2D materials. We have performed a statistical survey on more than 200 MnBi_2Te_4 exfoliated from four crystals grown by different groups, and the main results are summarized in Figs. 4a and 4b. The most striking observation is that most of the studied MnBi_2Te_4 flakes exhibit O_c reduction, although to different extents, which is never reported in previous studies of MnBi_2Te_4 . As presented in Fig. 4b, the blue and magenta dashed lines mark the area of O_c reduction of 0 and 20 %, respectively. The flakes situated close to the blue dashed line display little O_c change after device fabrication, whereas the flakes close to the magenta dashed line experience a pronounced O_c reduction, corresponding to an effective thickness decrease of 1 SL. The subtle increase of O_c in some certain samples is attributed to measurement error (see methods). In the top panel of Fig. 4a, we present the optical images of four typical MnBi_2Te_4 flakes, which clearly illustrate the pronounced color change caused in the fabrication process. In Fig. 4c, we further analyze the distribution of the O_c change for the different crystals. The leftward shift of the center of the blue lines clearly indicates that the impacts of the fabrication process on O_c are highly crystal-dependent. For most of the samples exfoliated from Crystal #1, their O_c values are only slightly affected. In contrast, almost all the flakes exfoliated from Crystal #4 exhibit significant reduction in O_c , corresponding to a thickness of 1 SL.

Discussion

Based on the above experimental observations, we discuss the possible explanations for the even-odd discrepancy of magnetotransport in few-layer MnBi_2Te_4 . It may be suspected that one physical layer is unintentionally removed during the fabrication process, leading to

an odd (even)-number-SL MnBi_2Te_4 to manifest transport behaviors that are characteristic of an even (odd)-number-SL MnBi_2Te_4 with 1 less SL^{24,25}. However, such scenario can be safely excluded. We performed atomic force microscopy measurement on the flakes exfoliated from the most sensitive crystal (#4). All these samples exhibit pronounced O_c reduction during the fabrication process (see supplementary section E), however their physical heights determined by atomic force microscopy remain unchanged. In supplementary section F, we also compare the variations in the magneto-optical Kerr effect (MOKE) and the coherent interlayer phonon frequency of two MnBi_2Te_4 before and after PMMA contact. It further demonstrates that the fabrication mainly affects the effective thickness rather than the physical thickness. Therefore, a more plausible scenario is that the change of O_c arises from the modification of the magnetic or electronic structures^{45,46,50}. In the experimental researches of MnBi_2Te_4 , it is a widespread phenomenon that MnBi_2Te_4 exhibits sample-dependent behaviors, whether between different crystals or different flakes exfoliated from the same crystal^{3,47,51}. A prevailing understanding attributes this to the various defects and the non-uniformity within MnBi_2Te_4 bulk crystal. It has been highlighted that the surface defects and the perturbations to the surface can result in instability of MnBi_2Te_4 (refs. 38,47,50-56). Given the intricate physical and chemical process involved in the fabrication process, we attribute the O_c variation to the fabrication-catalyzed instability of MnBi_2Te_4 surface.

It is worth noting that some imaging experiment and theoretical calculations have clearly identified some physical mechanisms that can result in a decrease of effective thickness. For instance, a scanning transmission electron microscopy imaging experiment demonstrated that the synergistic effect of a high concentration of Mn-Bi site mixing and Te vacancy can trigger a surface reconstruction process from one SL of MnBi_2Te_4 to a quintuple layer of $\text{Mn-Bi}_2\text{Te}_3$ and an amorphous double layer of $\text{Mn}_x\text{Bi}_y\text{Te}$ (ref. 50). As a result, the effective thickness for the MnBi_2Te_4 structure is reduced by 1-SL. Theoretical calculations also reveal that a surface charge redistribution process can relocate the surface state from the first SL to the second SL, resulting in the decrease of effective thickness for magnetotransport⁵¹. Recently, a theoretical work demonstrates that a small expansion of the interlayer van der Waals gap can result in a noteworthy reduction in the surface gap⁵⁶. Specifically, for a (7+1) SL MnBi_2Te_4 , it triggers

a topological phase transition with Chern number change by one. An odd (even)-number-SL MnBi_2Te_4 will naturally manifest magnetotransport properties akin to its even (odd)-number-SL counterpart with 1 less SL. Based on the sample-dependent defect type and concentration, as well as the susceptibility of MnBi_2Te_4 surface to perturbations^{47,48,50,51,56}, we hypothesize that the sample dependent behaviors observed during the fabrication arise from the PMMA-catalyzed surface instability. Notably, prior researches on graphene, MoS_2 , and WSe_2 indeed suggested that the PMMA residuals on the surface influence the intrinsic properties of the 2D materials⁵⁷⁻⁵⁹. It can not only increase the observed thickness in the atomic force microscopy measurement through absorption, but also act as charge source, prompting the surface charge redistribution. Our topography measurement has indeed shown island-like PMMA residuals on the MnBi_2Te_4 surface (see supplementary Fig. S8). In addition, various adsorbates trapped between layers during the fabrication can also expand the van der Waals gap⁶⁰. Therefore, it is likely that the combined influences of non-uniformity, defects, and PMMA contribute to the sample dependent behaviors in response to fabrication. Further studies are needed to fully understand the underlying mechanisms. In Figs. 4d and 4e, we display the process of effective thickness reduction with the magenta frame indicating the effective thickness for transport. The reduced gap elucidates the narrower V_g and T range of the zero Hall plateau for the 7-SL sample (S6).

While the precise mechanism through which PMMA influences the quality of MnBi_2Te_4 samples remains incompletely understood, a potential solution to circumvent such fabrication issue involves isolating PMMA from the surface during the fabrication. Building upon recent advancements in low-damage lithography in the QAH system^{35,37}, we suggest that depositing a thin layer of AlO_x on the surface of MnBi_2Te_4 prior to fabrication may alleviate the damage of PMMA. In supplementary section G, we present our preliminary results obtained in crystal #5, which demonstrates the efficacy of the modified method in addressing the current issue.

In addition to the zero Hall plateau in the 7-SL MnBi_2Te_4 device, the fabrication-induced mismatched layer dependent magnetotransport behaviors are also evident in MnBi_2Te_4 flakes with other thicknesses, as displayed in Figs. 4f and 4g. Among the seven samples, devices S1 and S5 were derived from crystals #3 and #2, respectively. All the other devices were derived

from crystal #1. Notably, those PMMA-insensitive MnBi_2Te_4 with less-affected O_c (blue stars in Fig. 4b) exhibit the anticipated behaviors for both even- and odd-number-SL MnBi_2Te_4 . In contrast, samples with pronounced O_c change (red stars in Fig. 4b) exhibit transport behaviors inconsistent with their nominal thickness. Specifically, as shown in Fig. 4g, odd-number-SL devices display vanished AH hysteresis in the AFM regime, while even-number-SL devices display hysteresis behaviors with counterclockwise chirality, as indicated by the black arrows. The AH effect with reversed chirality may arise from the electric field due to gate or substrate, or the competition between various intrinsic and extrinsic mechanisms^{23,32,33,48,61}. In addition to the Hall effect, since the transport of odd- and even-number-SL MnBi_2Te_4 are conducted by chiral and helical edge states^{13,39}, the fabrication-induced mismatched even-odd dependent magnetotransport should also be manifested by the nonlocal transport measurements, which are observed in our experiment (see supplementary section H for details).

We have conducted a comprehensive investigation of the transport properties in a large number of few-layer MnBi_2Te_4 flakes. By tracking the quantized Hall plateau with respect to $\mu_0 H$ and V_g , and comparing the optical properties before and after the fabrication process, our study elucidates the relationship between transport behaviors and device fabrication process. Our research has uncovered a condition in which the effective thickness for charge transport in MnBi_2Te_4 becomes decoupled from its pristine physical thickness, which is never reported in previous studies. Although the exact microscopic mechanism underlying the change of O_c remains to be determined, and we cannot exclude that those devices exhibiting unchanged O_c are not affected by fabrication because the AH effect ($0.1 h/e^2$) in odd-number-SL MnBi_2Te_4 is not quantized, our experiments still provide highly valuable insights for the fabrication of high-quality MnBi_2Te_4 toward realizing quantized phenomena. Our finding not only explains the controversies concerning the mismatched even-odd layer dependent magnetotransport in MnBi_2Te_4 , but also highlights the critical issues regarding the fabrication and characterization of devices based on 2D materials.

Methods

Crystal growth High-quality MnBi_2Te_4 single crystals were synthesized independently by different methods. For crystal #1, it was grown by directly mixing Bi_2Te_3 and MnTe with the ratio of 1:1 in a vacuum-sealed silica ampoule. After heated to 973 K, the mixture was slowly cooled down to 864 K, followed by a long period of annealing process. The phase and crystal structure were examined by X-ray diffraction on a PANalytical Empyrean diffractometer with $\text{Cu K}\alpha$ radiation. For crystal #2, it was grown by conventional flux method. Mn powders, Bi and Te were weighed with the ratio $\text{Mn:Bi:Te} = 1:8:13$ ($\text{MnTe:Bi}_2\text{Te}_3 = 1:4$) in an argon-filled glovebox. The mixtures were loaded into a corundum crucible which was sealed into a quartz tube. Then the tube was then put into a furnace and heated up to 1000 °C for 20 hours. After a quick cooling to 605 °C with the rate of 5 °C/h, the mixtures were then slowly cooled down to 590 °C with the rate of 0.5 °C/h and kept for 2 days. Finally, the crystals were obtained after centrifuging. For crystal #3, it was grown by the conventional high-temperature solution method. The Mn , Bi and Te blocks were weighed with a ratio of $\text{Mn:Bi:Te} = 1:11.3:18$, and placed in an alumina crucible, which were then sealed in a quartz tube in argon environment. The assembly was first heated up in a box furnace to 950 °C and held for 10 hours, and then cooled down to 700 °C within 10 hours and further cooled down to 575 °C in about 100 hours. After the heating procedure, the quartz tube was then taken out quickly and decanted into the centrifuge to remove the flux from the crystals. For crystal #4, it was grown by flux method using MnCl_2 as the flux. The raw materials of Bi_2Te_3 powder, Mn lump, Te lump and MnCl_2 powder were mixed with a molar ratio of 1:1:1:0.3 and then placed in a dry alumina crucible, which was sealed in a fused silica ampoule under vacuum. The ampoule was then placed in a furnace and heated up to 850 °C for over 20 hours, kept there for 24 hours, cooled down to 595 °C in over 5 hours, kept there for 150 hours, and finally cooled to room temperature in 5 hours. After the steps above, the yielded ingot was cleaved into millimeter-sized crystals with metallic luster. For crystal #5, it was grown by directly mixing Bi_2Te_3 , MnTe and Te with the ratio of 1:1:0.2 in a vacuum-sealed silica ampoule. The ampoule was slowly heated to 900°C at a rate of 3°C/min and maintained at this temperature for 1 hour. Subsequently, the sample was cooled at a rate of 3°C/min to 700°C, held at this temperature for 1 hour. The temperature

was then gradually decreased to 585°C at a rate of 0.5°C/min and maintained for annealing for 12 days. After the annealing process, the quartz ampoule was quenched in water to avoid phase impurities. Millimeter-sized MnBi_2Te_4 crystals were obtained after crushing the ingot.

Device fabrication MnBi_2Te_4 flakes were exfoliated onto 285 nm-thick SiO_2/Si substrates by using the Scotch tape method in an argon-filled glove box with O_2 and H_2O levels lower than 0.1 ppm. Before exfoliation, all SiO_2/Si substrates were pre-cleaned by air plasma for 5 minutes at ~ 125 Pa pressure. To minimize the experimental errors due to the subtle difference in measurement conditions, such as the position of the flakes in the light fields, the uniformity of illumination, the size and shape of the sample, and the presence of electrode, the O_c shown in the main text were calculated by averaging the O_c of different parts across the sample. For the transport devices, thick flakes around the target sample were first scratched off by using a sharp needle in the glove box. A layer of 270 nm PMMA was spin-coated before EBL and heated at 60 °C for 5 minutes. After the EBL, 23 to 53 nm thick Cr/Au electrodes (3/20 to 3/50 nm) were deposited by a thermal evaporator connected with an argon-filled glove box. Before the fabrication and sample transfer process, the devices were always spin-coated with a PMMA layer to avoid contact with air. All the seven devices (S1-S7) shown in the text were fabricated through the same process.

Transport measurement Four probe transport measurements were carried out in a cryostat with the lowest temperature 1.6 K and out-of-plane magnetic field up to 9 T. The longitudinal and Hall signals were acquired simultaneously via lock-in amplifiers with an AC current (200 nA, 13 Hz) generated by a Keithley 6221 current source meter. To correct for the geometrical misalignment, the longitudinal and Hall signals were symmetrized and antisymmetrized with magnetic field respectively. The back-gate voltages were applied by a Keithley 2400 source meter.

Scanning SQUID measurement Scanning SQUID measurements were carried in a different cryostat from the transport measurements. Scanning 2-junction SQUID susceptometers with two balanced pickup loops of 2 μm diameter in a gradiometric configuration were utilized as

the SQUID sensors. Each of them was surrounded by a one-turn field coils of 10 μm diameter. The DC flux was measured through the pickup loop using a voltage meter (Zurich Instrument HF2LI) as a function of position and reflects the intrinsic magnetization of the sample.

Polar MOKE measurement Polar MOKE measurements were carried using a 633 nm HeNe laser. After transmitting through a linear polarizer, the light was focused to a 2 μm spot on the sample by a reflective objective at normal incidence to avoid the large backgrounds that occur when a typical lens is used. The sample was mounted on a cold stage at 3 K within the vacuum chamber of an optical superconducting magnet system. The reflected beam is modulated at \sim 50 kHz by a PEM, split by a Wollaston prism, and detected using a balanced photodiode. The resulting 50 and 100 kHz modulations detected by lock-in amplifiers then correspond to the ellipticity and rotation angle of the beam respectively. We additionally modulate the intensity of the beam with a frequency of 2317 Hz chopper to measure the DC signal for normalization using a third lock-in.

Data Availability: All data supporting the finding in the study are presented within the main text and the supplementary information. All data are available upon reasonable request from the corresponding author.

References

1. Gong Y., Guo J. W., Li J. H., *et al.* Experimental Realization of an Intrinsic Magnetic Topological Insulator. *Chin. Phys. Lett.*, **36**, 076801 (2019).
2. Otrokov M. M., Klimovskikh I. I., Bentmann H., *et al.* Prediction and observation of an antiferromagnetic topological insulator. *Nature*, **576**, 416-422 (2019).
3. Deng Y., Yu Y., Shi M. Z., Guo Z., Xu Z., Wang J., Chen X. H., Zhang Y. Quantum anomalous Hall effect in intrinsic magnetic topological insulator MnBi_2Te_4 . *Science*, **367**, 895-900 (2020).
4. Ge J., Liu Y., Li J., Li H., Luo T., Wu Y., Xu Y., Wang J. High-Chern-number and high-temperature quantum Hall effect without Landau levels. *Natl Sci Rev*, **7**, 1280-1287 (2020).
5. Liu C., Wang Y., Li H., *et al.* Robust axion insulator and Chern insulator phases in a two-dimensional antiferromagnetic topological insulator. *Nat. Mater.*, **19**, 522-527 (2020).
6. Liu C., Wang Y., Yang M., *et al.* Magnetic-field-induced robust zero Hall plateau state in

- MnBi₂Te₄ Chern insulator. *Nat. Commun.*, **12**, 4647 (2021).
7. Qi X. L., Hughes T. L., Zhang S. C. Topological field theory of time-reversal invariant insulators. *Phys. Rev. B*, **78**, 195424 (2008).
 8. Mogi M., Okamura Y., Kawamura M., *et al.* Experimental signature of the parity anomaly in a semi-magnetic topological insulator. *Nat. Phys.*, **18**, 390+ (2022).
 9. Li J., Li Y., Du S., Wang Z., Gu B. L., Zhang S. C., He K., Duan W., Xu Y. Intrinsic magnetic topological insulators in van der Waals layered MnBi₂Te₄-family materials. *Sci. Adv.*, **5**, eaaw5685 (2019).
 10. Chang C. Z., Zhang J. S., Feng X., *et al.* Experimental Observation of the Quantum Anomalous Hall Effect in a Magnetic Topological Insulator. *Science*, **340**, 167-170 (2013).
 11. Yang S. H., Naaman R., Paltiel Y., Parkin S. S. P. Chiral spintronics. *Nat. Rev. Phys.*, **3**, 328-343 (2021).
 12. Chen R., Li S., Sun H. P., Liu Q. H., Zhao Y., Lu H. Z., Xie X. C. Using nonlocal surface transport to identify the axion insulator. *Phys. Rev. B*, **103**, L241409 (2021).
 13. Li Y., Liu C., Wang Y., *et al.* Giant nonlocal edge conduction in the axion insulator state of MnBi₂Te₄. *Sci Bull (Beijing)*, **68**, 1252-1258 (2023).
 14. Morimoto T., Furusaki A., Nagaosa N. Topological magnetoelectric effects in thin films of topological insulators. *Phys. Rev. B*, **92**, 085113 (2015).
 15. Wang J., Lian B., Qi X. L., Zhang S. C. Quantized topological magnetoelectric effect of the zero-plateau quantum anomalous Hall state. *Phys. Rev. B*, **92**, 081107 (2015).
 16. Nenno D. M., Garcia C. A. C., Gooth J., Felser C., Narang P. Axion physics in condensed-matter systems. *Nat. Rev. Phys.*, **2**, 682-696 (2020).
 17. Mogi M., Kawamura M., Tsukazaki A., Yoshimi R., Takahashi K. S., Kawasaki M., Tokura Y. Tailoring tricolor structure of magnetic topological insulator for robust axion insulator. *Sci. Adv.*, **3**, eaao1669 (2017).
 18. Mogi M., Kawamura M., Yoshimi R., Tsukazaki A., Kozuka Y., Shirakawa N., Takahashi K. S., Kawasaki M., Tokura Y. A magnetic heterostructure of topological insulators as a candidate for an axion insulator. *Nat. Mater.*, **16**, 516+ (2017).
 19. Xiao D., Jiang J., Shin J. H., *et al.* Realization of the Axion Insulator State in Quantum Anomalous Hall Sandwich Heterostructures. *Phys. Rev. Lett.*, **120**, 056801 (2018).
 20. Qiu J. X., Tzschaschel C., Ahn J., *et al.* Axion optical induction of antiferromagnetic order. *Nat. Mater.*, **22**, 583-590 (2023).
 21. Wang F., Wang X., Zhao Y. F., *et al.* Interface-induced sign reversal of the anomalous Hall effect in magnetic topological insulator heterostructures. *Nat. Commun.*, **12**, 79 (2021).

22. Ying Z., Zhang S., Chen B., Jia B., Fei F., Zhang M., Zhang H., Wang X., Song F. Experimental evidence for dissipationless transport of the chiral edge state of the high-field Chern insulator in MnBi_2Te_4 nanodevices. *Phys. Rev. B*, **105**, 085412 (2022).
23. Gao A., Liu Y. F., Hu C., *et al.* Layer Hall effect in a 2D topological axion antiferromagnet. *Nature*, **595**, 521-525 (2021).
24. Cai J. Q., Ovchinnikov D., Fei Z. Y., *et al.* Electric control of a canted-antiferromagnetic Chern insulator. *Nat. Commun.*, **13**, 1668 (2022).
25. Ovchinnikov D., Huang X., Lin Z., *et al.* Intertwined Topological and Magnetic Orders in Atomically Thin Chern Insulator MnBi_2Te_4 . *Nano Lett*, **21**, 2544-2550 (2021).
26. Zhao Y.-F., Zhou L.-J., Wang F., *et al.* Even–Odd Layer-Dependent Anomalous Hall Effect in Topological Magnet MnBi_2Te_4 Thin Films. *Nano Lett*, **21**, 7691-7698 (2021).
27. Chen B., Fei F., Zhang D., *et al.* Intrinsic magnetic topological insulator phases in the Sb doped MnBi_2Te_4 bulks and thin flakes. *Nat. Commun.*, **10**, 4469 (2019).
28. Liu C., Zang Y. Y., Gong Y., He K., Ma X. C., Xue Q. K., Wang Y. Y. Ambi-chiral anomalous Hall effect in magnetically doped topological insulators. *Sci China Phys Mech*, **65**, 266812 (2022).
29. Liu C., Zang Y., Ruan W., Gong Y., He K., Ma X., Xue Q. K., Wang Y. Dimensional Crossover-Induced Topological Hall Effect in a Magnetic Topological Insulator. *Phys. Rev. Lett.*, **119**, 176809 (2017).
30. Checkelsky J. G., Ye J. T., Onose Y., Iwasa Y., Tokura Y. Dirac-fermion-mediated ferromagnetism in a topological insulator. *Nat. Phys.*, **8**, 729-733 (2012).
31. Smejkal L., Mokrousov Y., Yan B. H., MacDonald A. H. Topological antiferromagnetic spintronics. *Nat. Phys.*, **14**, 242-251 (2018).
32. Zhang S., Wang R., Wang X., *et al.* Experimental Observation of the Gate-Controlled Reversal of the Anomalous Hall Effect in the Intrinsic Magnetic Topological Insulator MnBi_2Te_4 Device. *Nano Lett*, **20**, 709-714 (2020).
33. Mei R., Zhao Y.-F., Wang C., Ren Y., Xiao D., Chang C.-Z., Liu C.-X. Electrically Controlled Anomalous Hall Effect and Orbital Magnetization in Topological Magnet MnBi_2Te_4 . *arXiv*, arXiv:2303.06204 (2023).
34. Chen R., Sun H.-P., Gu M., Hua C.-B., Liu Q., Lu H.-Z., Xie X. C. Layer Hall effect induced by hidden Berry curvature in antiferromagnetic insulators. *Natl. Sci. Rev.*, 10.1093/nsr/nwac1140 (2022).
35. Andersen M. P., Rodenbach L. K., Rosen I. T., *et al.* Low-damage electron beam lithography for nanostructures on Bi_2Te_3 -class topological insulator thin films. *arXiv*, arXiv:2301.11900 (2023).
36. Tay H., Zhao Y.-F., Zhou L.-J., Zhang R., Yan Z.-J., Zhuo D., Chan M. H. W., Chang C.-Z. Environmental Doping-Induced Degradation of the Quantum Anomalous Hall

- Insulators. *Nano Lett*, **23**, 1093-1099 (2023).
37. Gao Z., Guo M., Lian Z., *et al.* Low-damage photolithography for magnetically doped (Bi,Sb)₂Te₃ quantum anomalous Hall thin films. *Chin. Phys. B*, **32**, 117303 (2023).
 38. Tan H., Yan B. Distinct Magnetic Gaps between Antiferromagnetic and Ferromagnetic Orders Driven by Surface Defects in the Topological Magnet MnBi₂Te₄. *Phys. Rev. Lett.*, **130**, 126702 (2023).
 39. Lin W. Y., Feng Y., Wang Y. C., *et al.* Direct visualization of edge state in even-layer MnBi₂Te₄ at zero magnetic field. *Nat. Commun.*, **13**, 7714 (2022).
 40. Bartram F. M., Leng Y. C., Wang Y. C., *et al.* Ultrafast coherent interlayer phonon dynamics in atomically thin layers of MnBi₂Te₄. *Npj Quantum Mater*, **7**, 84 (2022).
 41. Zhu J., Feng Y., Zhou X., *et al.* Direct observation of chiral edge current at zero magnetic field in odd-layer MnBi₂Te₄. p. arXiv:2307.10150; 2023.
 42. Sass P. M., Kim J., Vanderbilt D., Yan J. Q., Wu W. D. Robust A-Type Order and Spin-Flop Transition on the Surface of the Antiferromagnetic Topological Insulator MnBi₂Te₄. *Phys. Rev. Lett.*, **125**, 037201 (2020).
 43. Nevola D., Li H. X., Yan J. Q., Moore R. G., Lee H. N., Miao H., Johnson P. D. Coexistence of Surface Ferromagnetism and a Gapless Topological State in MnBi₂Te₄. *Phys. Rev. Lett.*, **125**, 117205 (2020).
 44. Li H., Gao S. Y., Duan S. F., *et al.* Dirac Surface States in Intrinsic Magnetic Topological Insulators EuSn₂As₂ and MnBi_{2n}Te_{3n+1}. *Phys. Rev. X*, **9**, 041039 (2019).
 45. Hao Y. J., Liu P. F., Feng Y., *et al.* Gapless Surface Dirac Cone in Antiferromagnetic Topological Insulator MnBi₂Te₄. *Phys. Rev. X*, **9**, 041038 (2019).
 46. Chen Y. J., Xu L. X., Li J. H., *et al.* Topological Electronic Structure and Its Temperature Evolution in Antiferromagnetic Topological Insulator MnBi₂Te₄. *Phys. Rev. X*, **9**, 041040 (2019).
 47. Garnica M., Otrokov M. M., Aguilar P. C., *et al.* Native point defects and their implications for the Dirac point gap at MnBi₂Te₄ (0001). *Npj Quantum Mater*, **7**, 7 (2022).
 48. Mazza A. R., Lapano J., Meyer H. M., *et al.* Surface-Driven Evolution of the Anomalous Hall Effect in Magnetic Topological Insulator MnBi₂Te₄ Thin Films. *Adv Funct Mater*, **32**, 2202234 (2022).
 49. Akhgar G., Li Q. L., Di Bernardo I., *et al.* Formation of a Stable Surface Oxide in MnBi₂Te₄ Thin Films. *Acs Appl Mater Inter*, **14**, 6102-6108 (2022).
 50. Hou F. C., Yao Q. S., Zhou C. S., *et al.* Te-Vacancy-Induced Surface Collapse and Reconstruction in Antiferromagnetic Topological Insulator MnBi₂Te₄. *Acs Nano*, **14**, 11262-11272 (2020).
 51. Shikin A. M., Estyunin D. A., Zaitsev N. L., *et al.* Sample-dependent Dirac-point gap in MnBi₂Te₄ and its response to applied surface charge: A combined photoemission and ab

- initio study. *Phys. Rev. B*, **104**, 115168 (2021).
52. Liu Y. H., Wang L. L., Zheng Q., *et al.* Site Mixing for Engineering Magnetic Topological Insulators. *Phys. Rev. X*, **11**, 021033 (2021).
 53. Yan J. Q. Perspective-The Elusive Quantum Anomalous Hall Effect in MnBi_2Te_4 : Materials. *ECS Journal of Solid State Science and Technology*, **11**, 063007 (2022).
 54. Hu C. W., Gao A. Y., Berggren B. S., *et al.* Growth, characterization, and Chern insulator state in MnBi_2Te_4 via the chemical vapor transport method. *Phys. Rev. Mater.*, **5**, 124206 (2021).
 55. Tan H. X., Yan B. H. Facet dependent surface energy gap on magnetic topological insulators. *Phys. Rev. B*, **105**, 165130 (2022).
 56. Wang D. H., Wang H. Q., Xing D. Y., Zhang H. J. Three-Dirac-fermion approach to unexpected universal gapless surface states in van der Waals magnetic topological insulators. *Sci China Phys Mech*, **66**, 297211 (2023).
 57. Jia Y. H., Gong X., Peng P., Wang Z. D., Tian Z. Z., Ren L. M., Fu Y. Y., Zhang H. Toward High Carrier Mobility and Low Contact Resistance: Laser Cleaning of PMMA Residues on Graphene Surfaces. *Nano-Micro Lett*, **8**, 336-346 (2016).
 58. Pirkle A., Chan J., Venugopal A., *et al.* The effect of chemical residues on the physical and electrical properties of chemical vapor deposited graphene transferred to SiO_2 . *Appl. Phys. Lett.*, **99**, 122108 (2011).
 59. Liang J. R., Xu K., Toncini B., Bersch B., Jariwala B., Lin Y. C., Robinson J., Fullerton-Shirey S. K. Impact of Post-Lithography Polymer Residue on the Electrical Characteristics of MoS_2 and WSe_2 Field Effect Transistors. *Adv Mater Interfaces*, **6**, 1801321 (2019).
 60. Haigh S. J., Gholinia A., Jalil R., *et al.* Cross-sectional imaging of individual layers and buried interfaces of graphene-based heterostructures and superlattices. *Nat. Mater.*, **11**, 764-767 (2012).
 61. Luo J., Tong Q., Jiang Z., *et al.* Exploring the Epitaxial Growth Kinetics and Anomalous Hall Effect in Magnetic Topological Insulator MnBi_2Te_4 Films. *Acs Nano*, **17**, 19022-19032 (2023).

Acknowledgements: Chang Liu (RUC) was supported by fundings from National Natural Science Foundation of China (Grant No. 12274453) and Open Research Fund Program of the State Key Laboratory of Low-Dimensional Quantum Physics (Grant No. KF202204). Jinsong Zhang was supported by funding from National Natural Science Foundation of China (Grants No. 12274252 and No. 12350404). Yayu Wang was supported the Basic Science Center Project of Natural Science Foundation of China (Grant No. 52388201), the New

Cornerstone Science Foundation through the New Cornerstone Investigator Program and the XPLOER PRIZE. Yayu Wang, Jinsong Zhang, and Chang Liu (RUC) acknowledge the financial support from Innovation program for Quantum Science and Technology (Grant No. 2021ZD0302502). Yang Wu was supported by funding from National Natural Science Foundation of China (Grants No. 51991340 and No. 51991343). Shuang Jia was supported by fundings from the National Natural Science Foundation of China (Grants No. 12225401 and No. 12141002), the National Key Research and Development Program of China Grant No. 2021YFA1401902. Chang Liu (SUSTC) was supported by funding from the National Natural Science Foundation of China (Grant No. 12074161). Tianlong Xia was supported by fundings from the National Natural Science Foundation of China (Grant No. 12074425), the National Key R&D Program of China (Grant No. 2019YFA0308602), and the Fundamental Research Funds for the Central Universities, and the Research Funds of Renmin University of China (No. 23XNKJ22). Yihua Wang acknowledge support by National Key R&D Program of China (Grant No. 2021YFA1400100), National Natural Science Foundation of China (Grant No. 12150003) and Shanghai Municipal Science and Technology Major Project (Grant No. 2019SHZDZX01). Luyi Yang was supported by fundings from the National Natural Science Foundation of China (Grants No. 12074212 and No. 12361141826).

Author contributions: C. L. (RUC), Y. Y. W. and J. S. Zhang supervised the research. C. L. (RUC), Y. X. L., Y. C. W., Z. C. L., L. C. X., Y. F., Y. Q. W, B. H. F, and S. Y. fabricated the devices and performed the transport measurements. Y. C. W., H. L., Y. W., H. W., T. L. X., R. E. L., C. L. (SUST), L. F. L and S. J. grew the MnBi_2Te_4 crystals. Y. C. W., Z. C. L., and Z. T. G performed the atomic force microscopy measurements. J. J. Z., Y. F. and Y. H. W. performed the scanning SQUID measurements. L. Y. L. and L. Y. Y. carried the MOKE measurements. C. L. (RUC), Y. X. L. and Y. Y. W. prepared the manuscript with comments from all authors.

Competing interests: The authors declare no competing interests.

Figure Captions

Fig. 1 | Crystal structure and basic calibration of few-layer MnBi_2Te_4 . a, Crystal structure

of an even-number-SL MnBi₂Te₄. **b**, Optical image of few-layer MnBi₂Te₄ flakes exfoliated on SiO₂/Si substrate. The numbers in the figure represent the O_c and the corresponding layer numbers. Here O_c is defined as $(I_{\text{flake}} - I_{\text{substrate}})/I_{\text{substrate}}$, where I_{flake} and $I_{\text{substrate}}$ are the intensity of MnBi₂Te₄ flake and substrate. **c**, Atomic force microscope morphology of the area marked by the dashed box in **b** and height profile of the MnBi₂Te₄ along the red line. **d**, Variation of O_c as a function of thickness. The numbers in parentheses represent the quantity of measured samples. The error bar is defined by the standard deviation of multiple measurements of the data. **e**, T dependence of ρ_{xx} for the 6- and 7-SL device measured at $\mu_0H = 0$ when E_{FS} are gated to the CNPs. The red and blue arrows mark the T_{NS} for AFM transition.

Fig. 2 | Distinct evolution of the zero Hall plateau for 6- and 7-SL MnBi₂Te₄ devices. a-b, V_g dependent ρ_{xx} and ρ_{yx} for the 6-SL (**a**) and 7-SL (**b**) device measured at $T = 1.5$ K. The black dashed lines denote the slope of ρ_{yx} in low-field AFM regime. For the 6-SL device, the zero Hall plateau exists in a wide V_g range from 36 to 49 V, while for the 7-SL device it only occurs in specific V_g around 13 V. The panels enclosed by thick magenta boundaries indicate the V_g regime where zero Hall phenomena exist.

Fig. 3 | V_g dependent transport properties and optical images for 6- and 7-SL MnBi₂Te₄ devices. a-b, ρ_{xx} (blue) and $d\rho_{yx}/dH$ (red) at $\mu_0H = 0$ as a function of V_g for the 6-SL (**a**) and 7-SL (**b**) device. For the 6-SL device, $d\rho_{yx}/dH$ changes sign from positive to negative at $V_g = 30$ V, followed by a broad zero Hall plateau with a range of 13 V. Whereas for the 7-SL device, $d\rho_{yx}/dH$ monotonously decreases and crosses zero at $V_g = 13$ V. There is no plateau formation near $d\rho_{yx}/dH = 0$. **c-d**, Colormaps of $d\rho_{yx}/dH$ as functions of μ_0H and V_g . The magenta dashed lines represent the zero Hall plateau regimes for the two devices. **e-f**, Optical images for the two devices acquired immediately after exfoliation and after fabrication. For the 6-SL device, O_c is less affected during the fabrication process, but for the 7-SL device O_c is significantly reduced from 12.5 to -0.2 %. The different colors of the electrodes in the two devices are due to the different thickness of Au, which does not affect conclusion on the effect of fabrication on O_c .

Fig. 4 | Statistical analysis of O_c for more than two hundred flakes and distinct thickness dependent transport properties. **a**, Optical images of four representative samples taken in a glove box right after exfoliation (top panel) and after the removal of PMMA (bottom panel). **b**, Summary of the O_c values of 223 MnBi_2Te_4 flakes after exfoliation and after the removal of PMMA. The blue and magenta dashed lines mark the O_c reduction by 0 and 20 %. Different colored dots represent the data acquired from different crystals. **c**, Distribution of O_c change in the four different crystals. For the most PMMA-sensitive crystal (#4), fabrication can give rise to O_c change corresponding to a thickness of 1 SL. **d-e**, Illustrations of the influence of PMMA on the surface electronic structure for a 7-SL MnBi_2Te_4 . **f-g**, Thickness dependent ρ_{yx} behaviors for MnBi_2Te_4 without (blue) and with (red) severe O_c change.

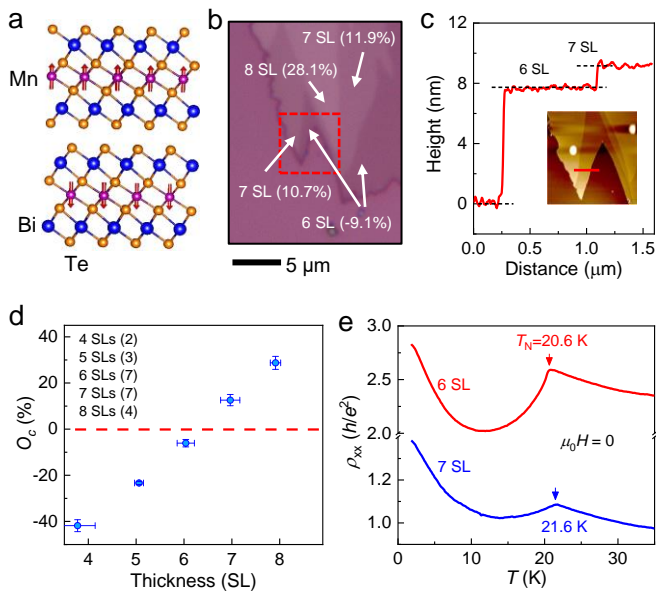


Figure 1

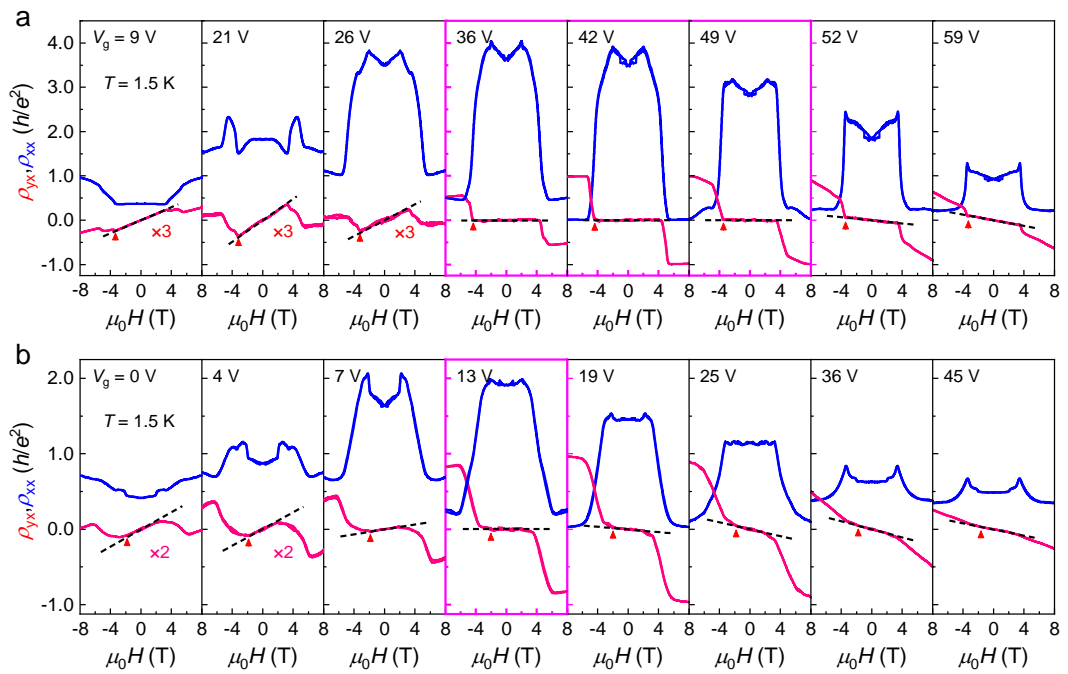


Figure 2

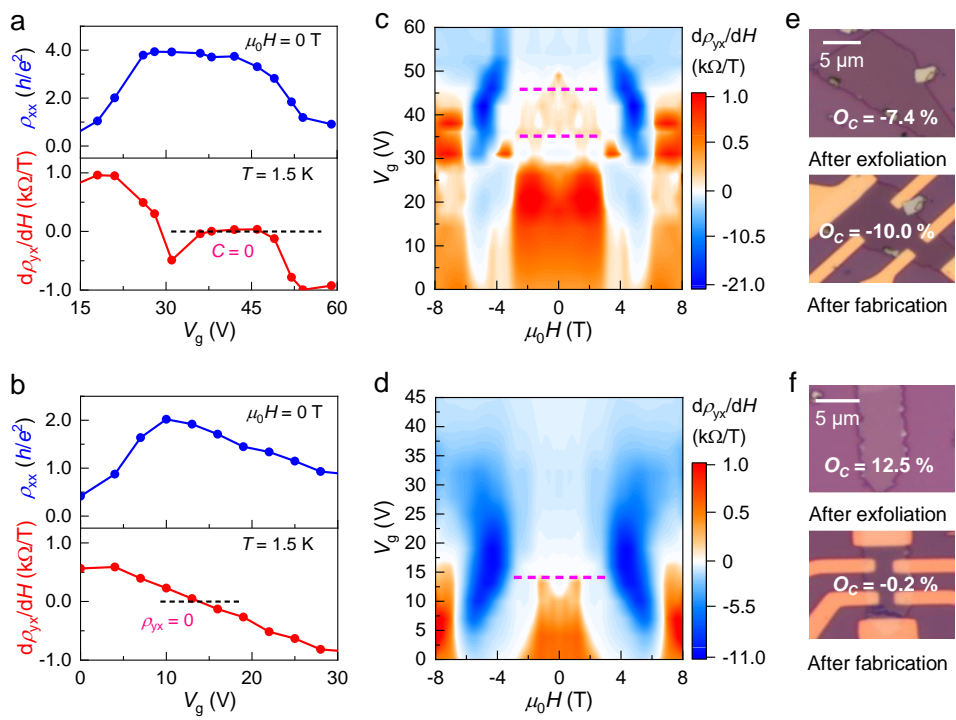


Figure 3

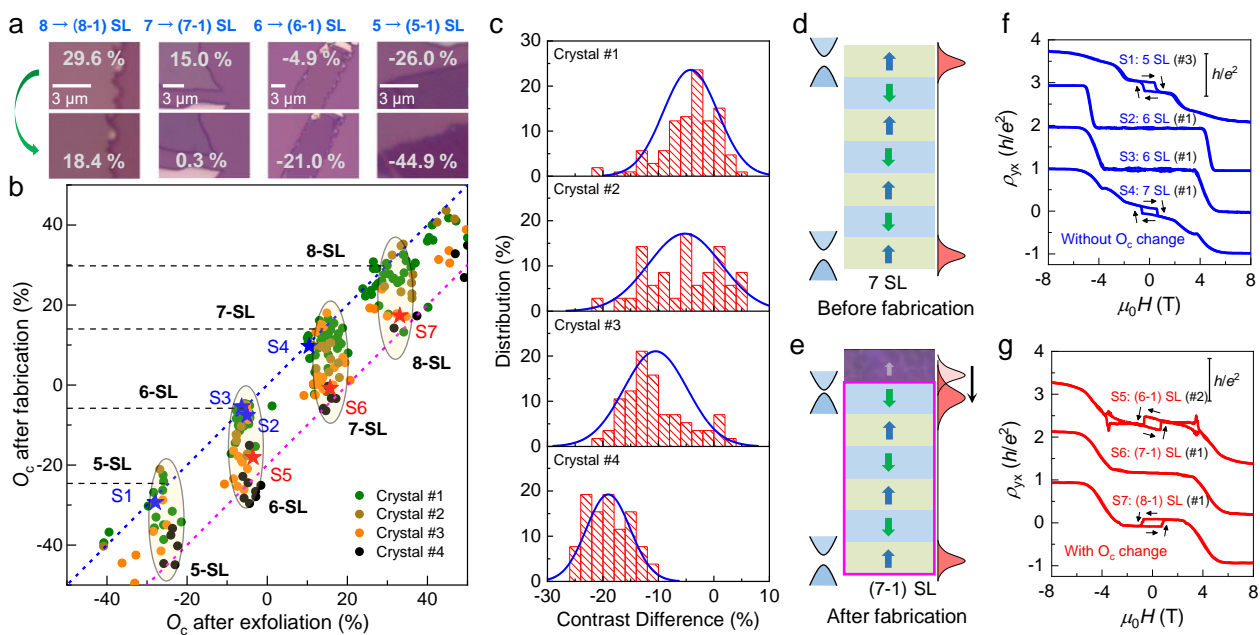


Figure 4